



Influence of rotation speed on interfacial bonding mechanism and mechanical performance of aluminum 6061 fabricated by multilayer friction-based additive manufacturing

Wenshen Tang¹ · Xinqi Yang¹ · Chaobo Tian¹

Received: 21 August 2022 / Accepted: 3 April 2023 / Published online: 13 April 2023
© The Author(s), under exclusive licence to Springer-Verlag London Ltd., part of Springer Nature 2023

Abstract

Friction-based additive manufacturing processes that allow the free design of the deposition path are expected to be used for the rapid production of large-scale high-performance aluminum alloy components. This study successfully fabricated multilayer deposits for 6061 aluminum alloy by friction extrusion additive manufacturing (FEAM) at a high deposition rate. The interfacial bonding properties and material utilization of the final deposits prepared at different rotational speeds were thoroughly investigated and evaluated based on the microstructural observations and mechanical test results. The multilayer deposition process was more stable and reliable at 400 rpm, and each layer was constant in width and thickness, approximately 32 mm wide and 4 mm thick. Planar interfaces were produced regardless of rotation speed, except that metal flow was more intense near the interface at 400 r/min in the driving friction zone, resulting in better interface formation and material utilization of 62.5%. The recrystallization fraction in the extrusion zone (EZ) of the fresh deposit at 400 r/min is 8.9% higher, and the deformation and recrystallization textures predominated in this region. After multiple thermal cycles and plastic deformation, dynamic recovery and subsequent static recovery occurred in the EZ, accompanied by subgrain coarsening and grain growth. Tensile properties in the build direction at 400 r/min are superior to those at 600 r/min, with tensile strength, 0.2% proof stress, and elongation after fracture being 47.4%, 32.0%, and 103% of the extruded 6061-T651 aluminum alloy, respectively.

Keywords Friction extrusion additive manufacturing · Additive friction stir deposition · Interface formability · Deposition efficiency · Microstructure · Mechanical properties

1 Introduction

Aluminum alloys are among the most extensively employed structural materials in industrial manufacturing due to their low density, high strength, exceptional corrosion resistance, fracture toughness, and plastic formability [1, 2]. Developments in metal additive manufacturing technologies offer new ways to design and rapidly fabricate complex lightweight aluminum structures freely [3, 4]. However, because of the inherent metallurgical limitations of aluminum alloys, including low melting point, susceptibility to thermal

cracking, and easy oxidation, it is challenging to achieve additively manufactured commercial aluminum alloy components without metallurgical defects such as porosity, cracks, and inclusions using fusion-based manufacturing processes [5–7].

Friction-based additive manufacturing (FAM) refers to a family of solid-state additive manufacturing methods created by merging layer-by-layer deposition and friction-based joining principles [8, 9]. Unlike existing fusion-based additive manufacturing processes, FAM does not entail the melting or solidification of the materials. It can therefore effectively overcome solidification defects that alloying, post-weld heat treatment, hot isostatic pressing or mechanical rolling cannot completely eliminate [8, 9]. The potential deployment of solid-state FAM technologies has been demonstrated in several experimental works, such as friction stir additive manufacturing (FSAM) [10–12], additive friction stir deposition (AFSD) [8, 13], hybrid metal extrusion and bonding (HYB)

✉ Xinqi Yang
xqyang@tju.edu.cn

¹ Tianjin Key Laboratory of Advanced Joining Technology, School of Materials Science and Engineering, Tianjin University, Tianjin, China

[14], friction rolling additive manufacturing (FRAM) [15], friction extrusion additive manufacturing (FEAM) [16, 17], friction stir powder additive manufacturing (FSPAM) [18], and wire-based FSAM (W-FSAM) [19]. The AFSD process developed by Aeroprobe Corporation offers significant advantages among all FAM processes regarding processing flexibility, deposition efficiency, production cost, and technological maturity. The company subsequently developed commercial 3D printing equipment based on AFSD, using the new term “MELD” to characterize this transformative process [8]. As the commercial devices of MELD continued to be introduced, researchers began to look in-depth at the fundamental issues of application for the MELD process. Currently, magnesium alloys [13], aluminum alloys [20, 21], pure copper, copper alloys [22, 23], nickel-based alloys [24], and titanium alloys [25] have been successfully investigated using the MELD process. However, the thickness of each deposited layer for aluminum alloy documented so far was around 1 mm, and the overall thickness of a single multilayer deposit seldom surpassed 6 mm [21, 23, 26–28]. In addition, the effects of repeated thermal cycling and plastic deformation on interface deformability and bonding quality have rarely been reported. In particular, there is no systematic evaluation of the joining efficiency and the material utilization of the multi-layer deposited components produced by the MELD process.

The FEAM process was achieved by a novel force-controlled spindle feed mechanism independently developed in China, allowing for a maximum thickness of 4 mm for single-layer deposition and a maximum diameter of 20 mm for feedstock rod [16, 17]. To emphasize the inherent feature of this deposition method and separate it from AFSD, we named it FEAM. The previous study [16] reported that a two-layer deposition of a 6061 aluminum alloy with a featureless shoulder was successfully fabricated in a single pass using the FEAM process. The finished part exhibited significant microstructural heterogeneity throughout its thickness, and the interface showed the most significant decrease in hardening precipitates as it was subjected to the highest temperature and the most plastic deformation [16]. However, further investigation and evaluation of the influence of processing parameters on the multilayer deposition process are required.

Solid-state additive manufacturing, such as ultrasonic additive manufacturing (UCS) and cold spray additive manufacturing (CSAM), is superior to fusion-based additive manufacturing in terms of a deposition rate. However, the bonding strength along the thickness accumulation direction in the as-printed state was poor, and the elongation at break was less than 0.2% [6, 29]. FAM processes that allow the accessible design of the deposition path have greatly improved processing flexibility and performance improvement [8]. However, there are also some deficiencies, such as

poor material utilization compared to fusion-based additive manufacturing. FEAM has demonstrated that the fabrication of 6061 aluminum alloy components was feasible with a much faster deposition rate than the MELD process [16, 17]. However, several critical aspects have not been thoroughly investigated, such as the bonding mechanism, microstructure features, plastic deformability at interfaces, and the width of effective bonding of multilayer deposits.

To investigate and evaluate the forming characteristics and plastic deformability of interfaces produced by friction-based additive manufacturing at high deposition rates, single-pass, nine-layer 6061 Al alloy components were first fabricated by the featureless shoulder-aided FEAM process at different rotation speeds. Thorough research and analysis were then carried out on the effect of rotation speed on the interface formability, mechanical properties, and joining efficiency of the final deposits.

2 Materials and methods

This study utilized a commercial extruded bar of 6061-T651 aluminum alloy with a nominal diameter of 20 mm as the starting material. Its chemical composition (wt%) is Al–0.9 Mg–0.54Si–0.28Cu–0.1Fe–0.04Ti–0.18Cr–0.12Mn. The substrate used for the experiments was a 5-mm-thick plate of 6061-T6 aluminum alloy.

The experiments were completed by using special solid-state FEAM equipment independently developed by Tianjin University. Figure 1(a) displays the schematic representations of the FEAM process. The deposition process ran at tool rotation speeds of 400 r/min and 600 r/min with a 300 mm/min constant traverse speed. The axial force acting on the feed rod of the consumable material was 10 kN. Each layer was fabricated using the same deposition direction. The final builds, with a length of 320 mm, consisted of 9 layers with a thickness of 4 mm each. The three-dimensional space of the additively manufactured components was described using three directions (see Fig. 1(a)): *X* is the direction of tool traverse (also known as the deposition direction), *Y* is the breadth direction of the deposited samples, and *Z* is the build direction (also known as the thickness accumulation direction of the final builds). The specific parameters used to deposit are listed in Table (1).

The metallographic specimens were examined using an optical microscope (OM, Axio Vert. A1, Carl Zeiss). The over-etching approach was utilized to disclose the material flow traces in various sections of the deposited layer and to investigate the interface bonding features. The microstructural features at different regions of the finished parts produced under different rotation speeds were quantitatively investigated using an electron backscatter diffractometer (EBSD, Zeiss Sigma 300-SEM with a Bruker Quantax EBSD detector). The grain

Fig. 1 Schematic representations of the FEAM process (a); the appearance of the final deposits at 400 r/min (b) and 600 r/min (c); tensile samples were taken along the build direction and their dimensions (d)

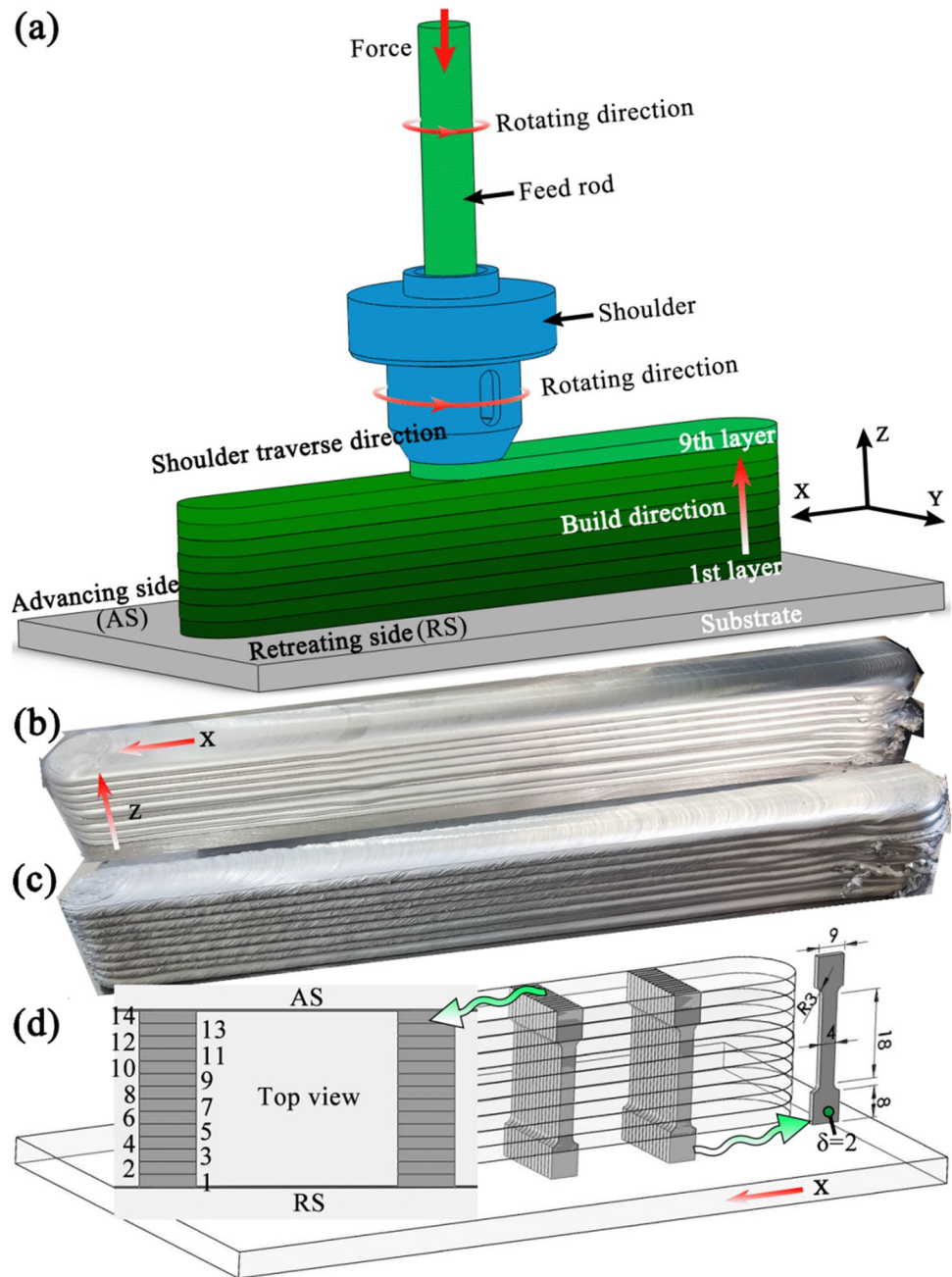


Table 1 Details of FEAM parameters used or recorded in this study

Deposition test no	Tool rotation speed (r·min ⁻¹)	Tool traverse speed (mm·min ⁻¹)	Tool pre-set thickness (mm)	Tool axial force (kN)
1	400	300	4	10
2	600	300	4	10

reconstruction method was applied to estimate grain size. Here, the grains at scan borders were not in the statistics. The proportions of recrystallized, substructured, and deformed

grains were calculated using HKL Channel 5 software and a discriminating approach proposed in a previous study [30]. In order to better understand the deposition process, the types and volume fractions of textures were also identified and estimated using orientation distribution functions (ODFs) and orientation maps within a cut-off angle of 15°.

Vickers microhardness tests were carried out along the build direction using a digital display durometer (HVS-1000) and a load of 0.98 N for 15 s. The specimens for the tensile tests were obtained in the build direction, and their dimensions are indicated in Fig. 1(d). Tensile samples were taken from the RS to the AS of the final deposits. These

specimens were used to investigate the bonding strength of the multilayer deposits. Numbers (No.) 1 through 14 were used to designate these samples for the convenience of comprehension (Fig. 1(d)). Microtensile testing equipment (INSTRON 2710–004) was used to conduct the tensile tests under a constant crosshead speed of 0.3 mm/min. The dimensions of the tensile specimens (Fig. 1(d)) and the tensile tests were performed in line with the standard ISO 6892–1:2019 [31].

3 Results

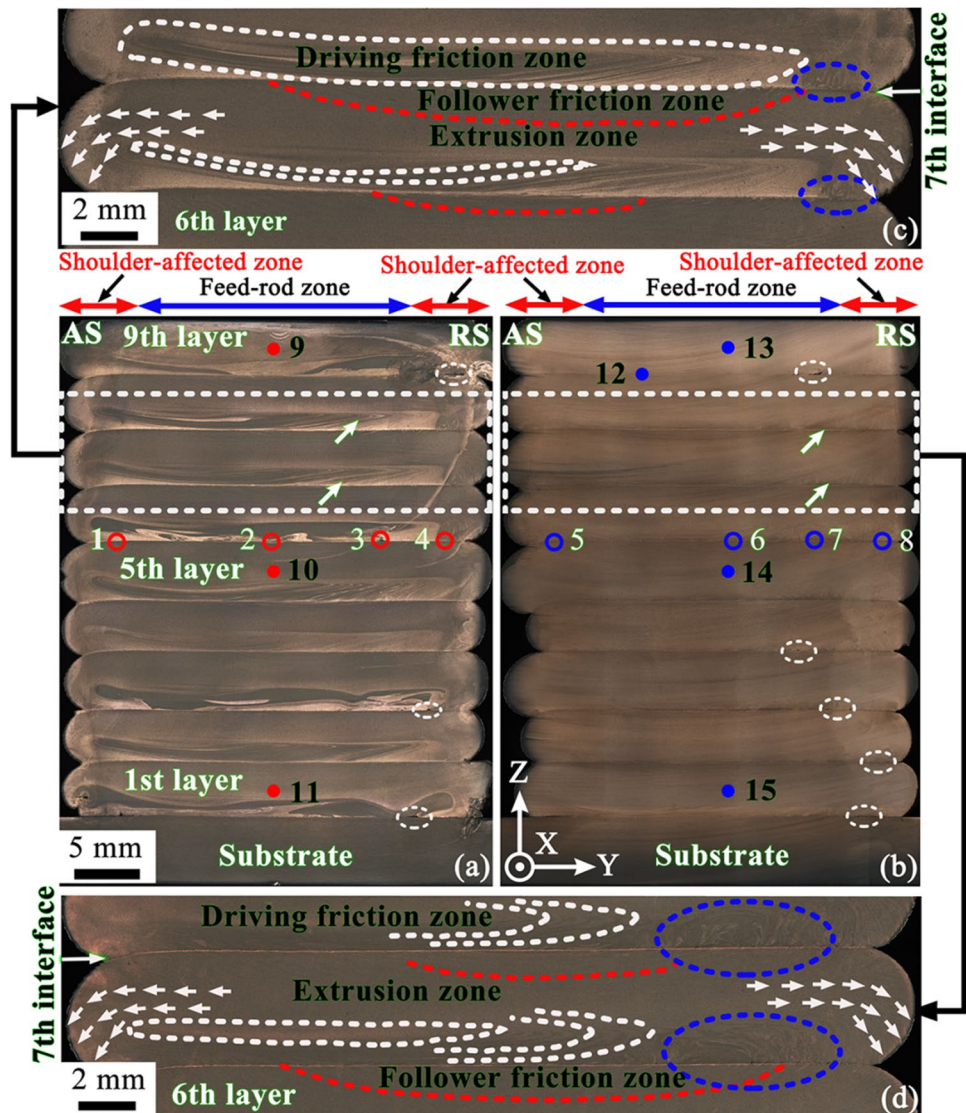
3.1 Macrostructure

The exterior appearance of the final deposits with nine layers generated at 400 and 600 r/min, as shown in Fig. 1(b) and (c), can be used to evaluate the stability and dependability

of the deposition process. Regardless of rotation speed, the surface of the final deposits remains smooth and defect free. Due to the effect of the rotating shoulder, the arc-shaped corrugation on the surface is clearly visible, comparable to that generated by friction stir welding [32–34]. Deposition at 400 r/min should be more stable, giving a more uniform width and a smoother surface (Fig. 1(b)). In comparison, the width of the final deposits at 600 r/min is significantly greater at the front end than at the rear end, with an increasingly rough second half on the retreating side (RS) (Fig. 1(c)). The differences in exterior appearance could be due to the fact that the effective torque experienced by the consumed feed rod is larger at a lower rotation speed [35, 36]. The increased effective torque allows the plasticized metal to flow more freely during deposition, resulting in smoother formation.

The macromorphology of the cross-section in final deposits produced at different rotation speeds is shown in Fig. 2. The widths of the nine layers deposited at 400 r/min are

Fig. 2 Cross-section of the final deposits in a macro view at 400 r/min (a, c) and 600 r/min (b, d), and a more detailed view of the sixth and seventh interfaces (c, d)



fairly uniform, each being about 32 mm wide and 4 mm thick (Fig. 2(a)). However, at 600 r/min, the first, second, and fourth layers are only 30 mm wide, whereas the remainder of the deposited layers can be up to 32 mm wide and up to 4 mm thick (Fig. 2(b)). In addition, although reasonably straight interfaces with little plastic deformation form at both rotation speeds, there are significant differences in metal flow within these interfaces, as indicated by the white arrowheads in Fig. 2(a) and (b).

The sixth and seventh interfaces produced at two rotation speeds are examined in more detail, as shown in Fig. 2 (c) and (d). The metal exhibits three distinct flow characteristics, as can be seen from the interface deposited at 400 r/min (Fig. 2(c)). The plasticized materials above the frictional interface between the newly deposited layer and the previous layer flow strongly, forming a flow pattern consisting of numerous layered eccentric elliptical rings, as indicated by the white dotted lines in Fig. 2(c). The oval rings are about 1/3 as thick as the single deposited layer. The region in which this flow takes place is referred to as the driving friction zone (DFZ) because it is created by the frictional shearing of the plasticized metal, which is actively driven by the consumable feed rod and the rotating shoulder. However, the metal underneath the frictional interface is subjected to frictional shearing twice as a new interface develops. Firstly, the surface of the deposited layer is directly affected by the frictional shearing of the rotating shoulder to produce the arcuate features. Secondly, this region is exposed to the direct frictional shearing of the plasticized materials when the next layer is deposited. As shown by the red dotted lines in Fig. 2(c), the area composed of the flow features with numerous layered semi-circular rings produced by the two forced frictional shearing effects is referred to as the follower friction zone (FFZ). In addition, the force exerted by the

feed rod and the rotating shoulder through the FFZ during the deposition process is primarily applied to the plasticized metal between the DFZ and the FFZ. The extrusion loading is expected to cause these metals to be extruded from the semi-enclosed space between the rotating shoulder and the substrate or previous layer, forming an extrusion zone (EZ). The flow path of the metal in the EZ, which is approximately 1/3 the thickness of the single deposited layer, is indicated by the white arrowheads in Fig. 2(c). It should be noted that the DFZs within the shoulder-affected zone at RS are poorly formed, and void defects are discovered in these locations, as illustrated in white and blue oval-dotted frames in Fig. 2(a) and (c), respectively. These defects have similar characteristics and fail to form complete flow rings as shown by the white dotted line in Fig. 2(c), presumably due to the moderate friction shearing impact of the rotating shoulder.

The interface generated at 600 r/min likewise displayed comparable metal flow characteristics, as depicted by the white and red dotted lines in Fig. 2(d). However, the flow rings of the plasticized materials produced in the DFZ were clearly shifted toward the advancing side (AS), and the interface with hole defects on the RS became much broader, as shown by the white and blue elliptical dashed frames in Fig. 2(b) and (d), respectively.

A more detailed view of the fifth interface produced at two rotation speeds is shown in Fig. 3. Material flow traces are clearly visible in the DFZ and FFZ, as indicated by the red and blue dotted lines. It should be noted that a good metallurgical bond appears to be achieved at the observation point in the center of the interface (Fig. 3(b) and (f)). In the DFZ, the hole defects are clearly visible. The kissing bond mentioned in earlier work [16] was also identified at the interface between the DFZ and the FFZ in the shoulder zone and the areas adjacent to the feed rod zone.

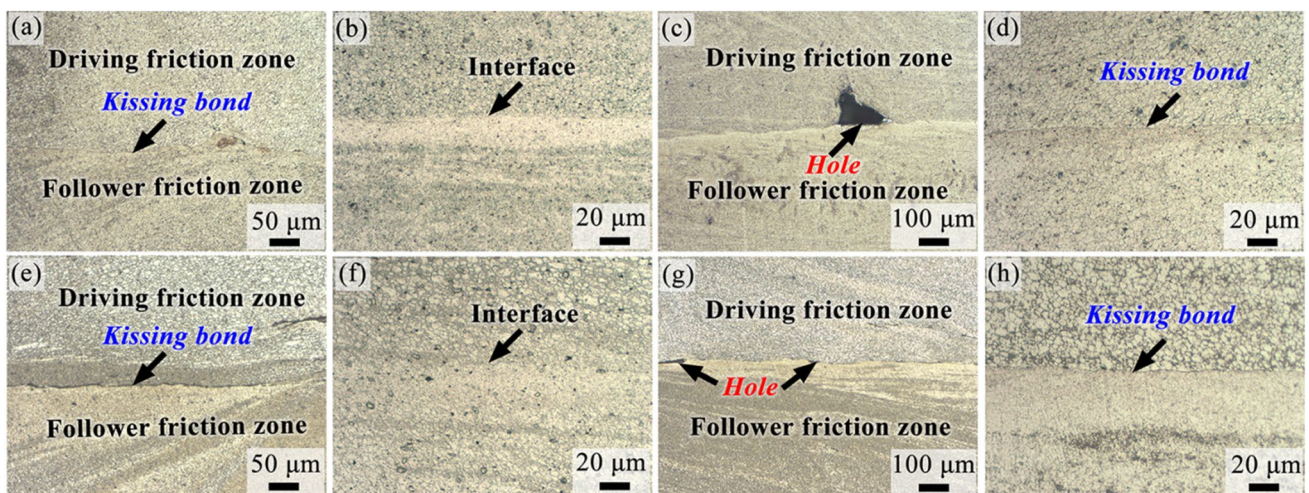


Fig. 3 Macro-view at various zones of the interface in magnification; **a** point 1, **b** point 2, **c** point 3, **d** point 4, **e** point 5, **f** point 6, **g** point 7, and **h** point 8 as designated in Fig. 2(a) and (b)

3.2 Microstructure

The ninth interface at 600 r/min was selected as a representative one to illustrate the microstructural features of DFZ and FFZ, as shown in Fig. 4. The detected zone (see point 12 in Fig. 2(b)) was located at AS and approximately 5 mm from the center of the ninth layer. Grain size, proportions of HABs and recrystallization, and volume fraction of the textures in DFZ and FFZ within the observed area were counted, and the results are given in Tables 2 and 3, respectively. A considerable dynamic recrystallization process with a recrystallization fraction of 82.3% occurred in DFZ within the ninth layer. Significantly refined equiaxed grains with an average grain size of about $4.4 \pm 1.9 \mu\text{m}$ were produced, although this region was only exposed to the effect of thermo-mechanical coupling once. In contrast, FFZ within the eighth layer was first subjected to the frictional shearing action of the non-consumable rotating shoulder while

depositing the eighth layer, followed by the frictional and extrusion action of the plasticized metal while depositing the ninth layer. A coarse-grained zone with a width of 20–40 μm formed near the bonding interface (Fig. 4(a)), with grain sizes ranging from 15 to 27 μm . The total recrystallization fraction of DFZ in the eighth layer is 70.9%, and the average grain size is $7.5 \pm 5.9 \mu\text{m}$.

Under different thermo-mechanical coupling effects, the type and content of the textures in DFZ and FFZ also changed (Fig. 4 (c) and (d)). Grains in DFZ were mainly dominated by recrystallized textures such as cube_{RD} ($\{013\} \langle 100 \rangle$), cube (C, $\{001\} \langle 100 \rangle$), and cube_{ND} (C_{ND} , $\{013\} \langle 100 \rangle$), the deformation textures such as S ($\{123\} \langle 634 \rangle$) and brass ($\{011\} \langle 112 \rangle$), and shear textures such as rotated Cu (RtCu, $\{112\} \langle 011 \rangle$) and B/\bar{B} ($\{111\} \langle 011 \rangle$). However, shear textures such as RtCu, B/\bar{B} and rotated goss (RtG, $\{011\} \langle 011 \rangle$) and deformation textures such as S and brass predominated in FFZ.

Fig. 4 Image quality map overlaid on grain boundaries (a), distribution maps of recrystallized (in blue), substructured (in yellow), and deformed (in red) grains (b), and orientation distribution functions (ODFs, c, and d) in the ninth interface at 600 r/min (point 12 labeled in Fig. 2(b)). The white-dotted line in (a) represents the bonding interface

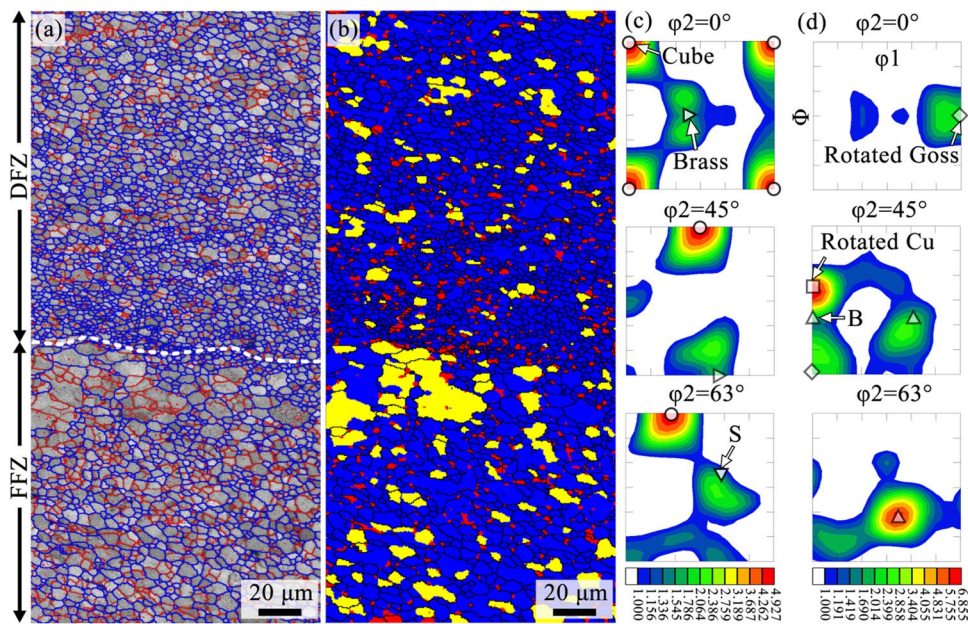


Table 2 Grain size and proportions of HABs and recrystallization of final deposits

Rotation speed	Regions	Grain size/ μm	HABs/%	Recrystallized/%	Substructured/%	Deformed/%
400 r/min	9th layer	5.3 ± 2.5	76.6	72.7	26.4	0.9
	5th layer	7.0 ± 4.3	62.9	59.5	39.8	0.7
600 r/min	1st layer	5.7 ± 3.0	67.0	63.2	35.8	1.0
	9th layer	6.9 ± 4.0	66.0	63.0	35.9	1.1
	5th layer	8.9 ± 3.6	73.3	69.0	30.7	0.3
	1st layer	9.2 ± 6.1	64.0	61.8	37.9	0.3
	DFZ (8th interface)	4.4 ± 1.9	74.3	82.3	9.3	8.4
FFZ (8th interface)	7.5 ± 5.9	60.1	70.9	22.3	6.8	

Table 3 Volume fractions of orientations in final deposits within a cut-off angle of 15° [37–39]

Rotation speed	Regions	Deformation textures						Shear textures			Recrystallization textures				
		S	T	Goss	{011} <811>	Cu	Brass	RtCu	RtG	B/B	C	C _{RD}	C _{ND}	F	P
400 r/min	9th layer	4.3	8.5	4.3	3.7	-	-	-	-	-	-	8.2	4.4	15.8	-
	5th layer	6.4	12.4	11.5	14.3	11.3	-	-	-	-	-	-	-	10	-
	1st layer	-	13.2	9.9	14.6	6.8	-	-	-	-	-	-	-	8	-
600 r/min	9th layer	7.2	12.5	15.9	10.9	7.8	-	-	-	-	-	6.2	-	-	-
	5th layer	-	7.2	6.7	7.6	6.5	-	-	-	-	-	-	-	4	-
	1st layer	3.8	6	-	5.4	-	-	-	-	-	-	-	-	17	8.9
	DFZ	9.5	-	-	-	-	4.6	5	-	3.9	6.2	7.4	4.3	-	-
	FFZ	4.6	-	-	-	-	3.6	15.7	5.2	6.5	-	-	-	-	-

Figure 5 shows the microstructural features of EZ in the first, fifth, and ninth layers of the final deposits produced at different rotation speeds. The grain size, proportions of HABs and recrystallization, and volume fraction of the

textures within EZ were counted, and the results are given in Tables 2 and 3, respectively. The thermo-mechanical coupling effect of EZ was greatly reduced compared to DFZ in the ninth layer at 600 r/min. The number of subgrains

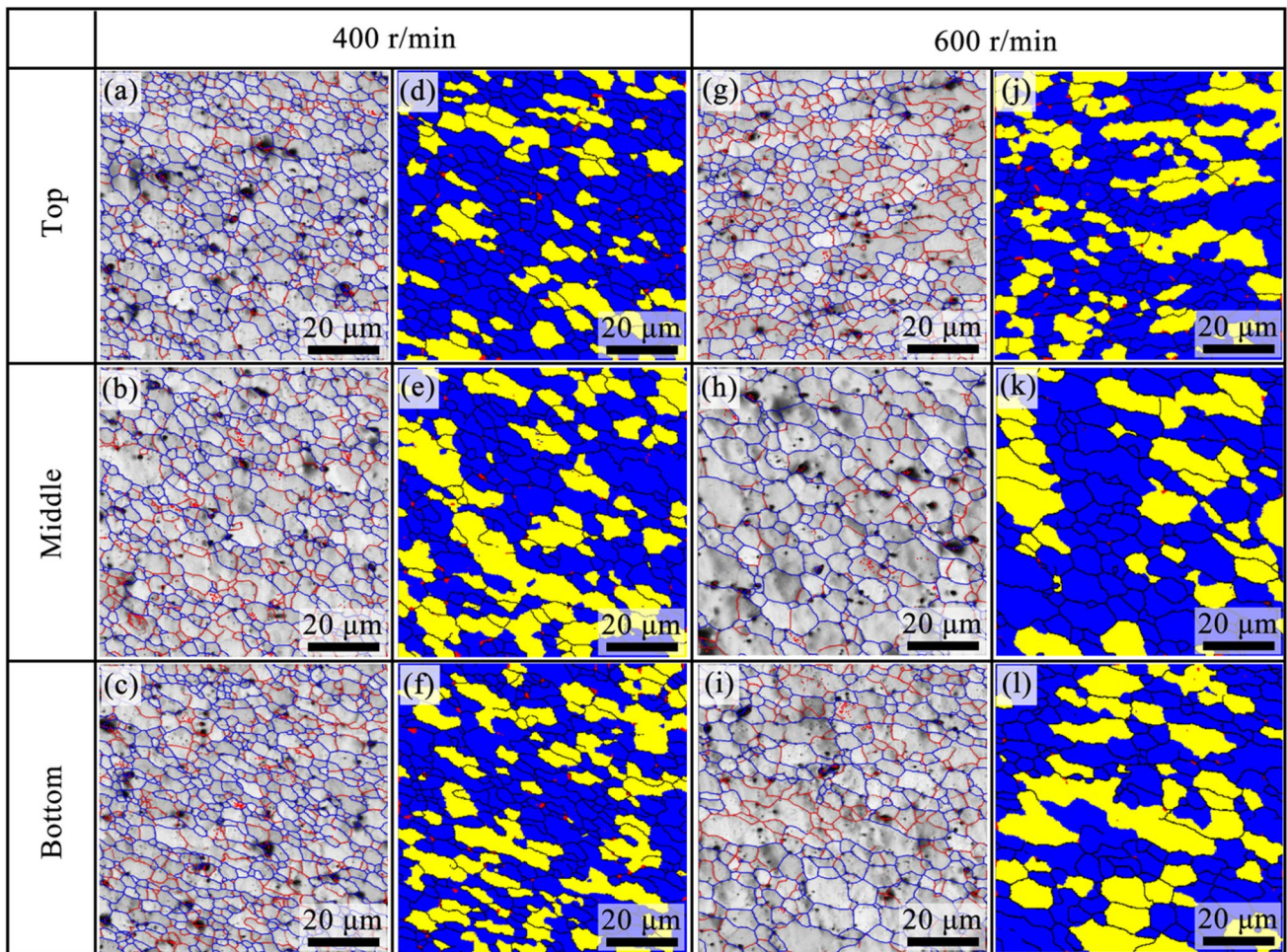


Fig. 5 Image quality maps (a–c and g–i) overlaid on grain boundaries and distribution maps (d–f and j–l) of recrystallized (in blue), substructured (in yellow), and deformed (in red) grains in extrusion

zones of final deposits at 400 r/min and 600 r/min; a, d point 9, b, e point 10, c, f point 11, g, j point 13, h, k point 14, i, l point 15 labeled in Fig. 2(a) and (b)

was considerably enhanced in this region. In contrast, the recrystallization fraction dropped significantly to 63.0%, and almost no deformed grains were formed (Fig. 5 and Table 2). Even after several thermal cycles and plastic deformation, the microstructure under both rotation speeds in EZ remained refined grains at both rotation speeds. The average grain size of EZ in the first, fifth and ninth layers obtained at 400 r/min was refined to 24.9%, 30.6%, and 23.1% of the starting material ($22.9 \pm 11.5 \mu\text{m}$ [16]), respectively. However, at 600 r/min, these values reached 40.2%, 38.9%, and 30.1% of the consumable feed rod, respectively. Grains in the ninth layer were highly refined by dynamic recrystallization after one thermal cycle and plastic deformation, whereas grain size in the first and fifth layers increased slightly after five and nine thermal cycles and plastic deformation. The average grain size of EZ at 400 r/min is about $6.0 \pm 3.3 \mu\text{m}$, while the grain size ($8.3 \pm 4.0 \mu\text{m}$) at 600 r/min is much larger. The variance in grain size is most likely due to the different recrystallization processes caused by the peak temperature and plastic deformation at both rotation speeds.

Figure 6 shows ODFs in extrusion zones of final deposits at 400 r/min and 600 r/min. Compared to DFZ and FFZ, grains in EZ were mainly dominated by deformation textures and recrystallization textures, with no shear texture present regardless of rotation speed and detection location. EZ in the ninth layer at 400 r/min was mainly dominated by $F(\{111\} \langle 112 \rangle)$, C_{RD} , and $T(\{213\} \langle 111 \rangle)$ components, with a peak intensity of 7.015. The same region at 600 r/min was mainly governed by deformation textures such as goss ($\{011\} \langle 100 \rangle$), T, Cu ($\{112\} \langle 111 \rangle$), S, and $\{011\} \langle 811 \rangle$ orientations with a maximum intensity of

12.608. After multiple thermal cycles and plastic deformation, the fraction of the deformation textures in EZ at 400 r/min grew noticeably, accompanied by a large increase in the maximum intensity of textures. However, the peak intensities of textures in the fifth and ninth layers at 600 r/min were dramatically lowered, as was the fraction of deformation texture. The first layer in EZ at 600 r/min was mainly dominated by recrystallized textures such as F and P ($\{011\} \langle 566 \rangle$) components.

3.3 Mechanical properties

Figure 7 shows the distribution of microhardness and statistical results of the specimens with nine layers produced at different rotation speeds. The newly deposited metal (the ninth layer) has much greater hardness than the previously deposited layers both in the center and on AS and RS of the deposited layers. The hardness of the deposited layer decreased steadily and remained constant in the seventh layer and below as the number of thermal cycles and plastic deformation increased. This reveals that, after a certain number of heat cycles, the hardness of the deposited layer is no longer affected by the newly formed layer, and the effect of precipitation hardening is no longer reduced. The average hardness values at the center, AS, and RS of the deposition layers produced at 400 r/min can reach 48.8%, 51.6%, and 52.5% of the starting material (113.1 HV [16]). However, the average hardness values of the same regions at 600 r/min are 49.7%, 51.6%, and 48.5% of the consumable base metal.

Figure 8(a) shows the engineering stress–engineering strain curves of no. 6 and no. 11 in one set of the test samples

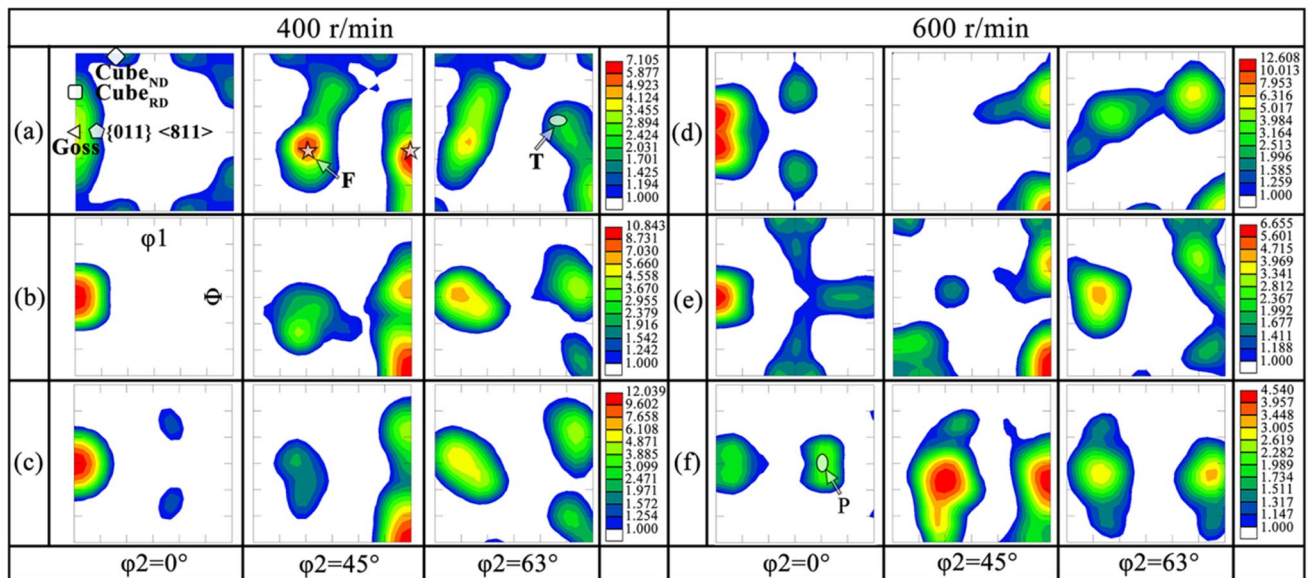


Fig. 6 ODFs in extrusion zones of final deposits at 400 r/min and 600 r/min; **a** point 9, **b** point 10, **c** point 11, **d** point 13, **e** point 14, **f** point 15 labeled in Fig. 2(a) and (b)

Fig. 7 Hardness profiles along the build directions on the AS (a), middle (b), and RS (c) in the cross-section of the final deposits at 400 r/min and 600 r/min, as well as the calculated average values (d)

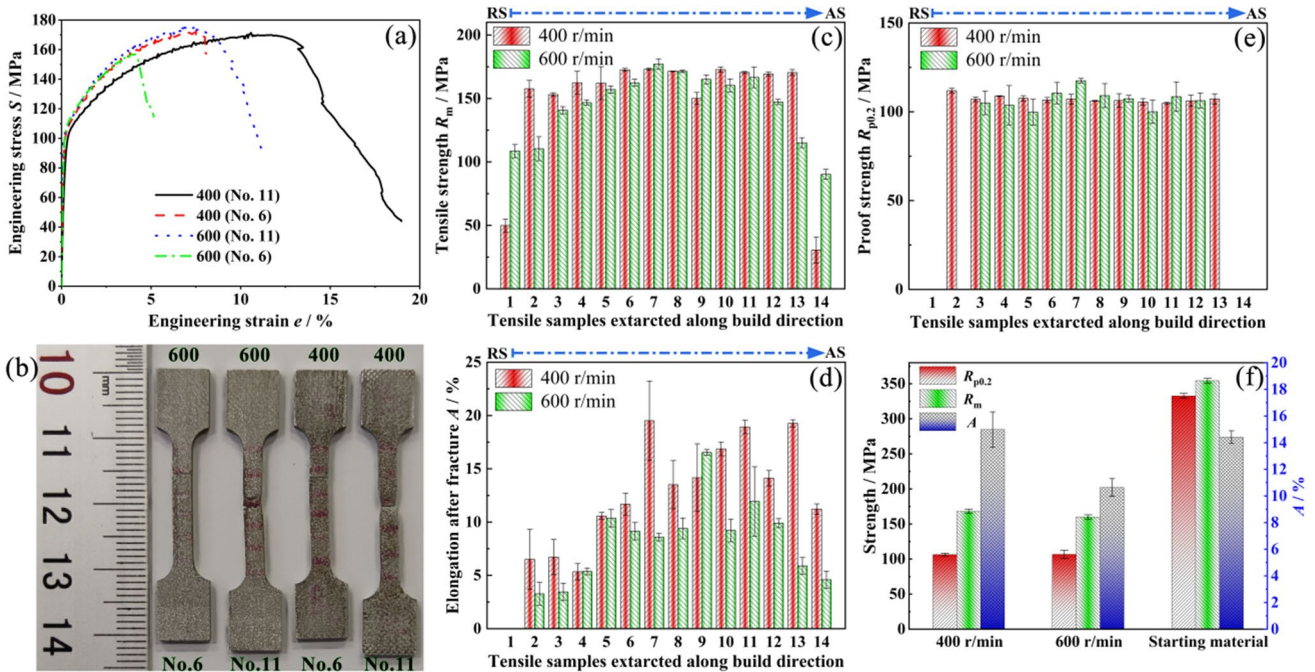
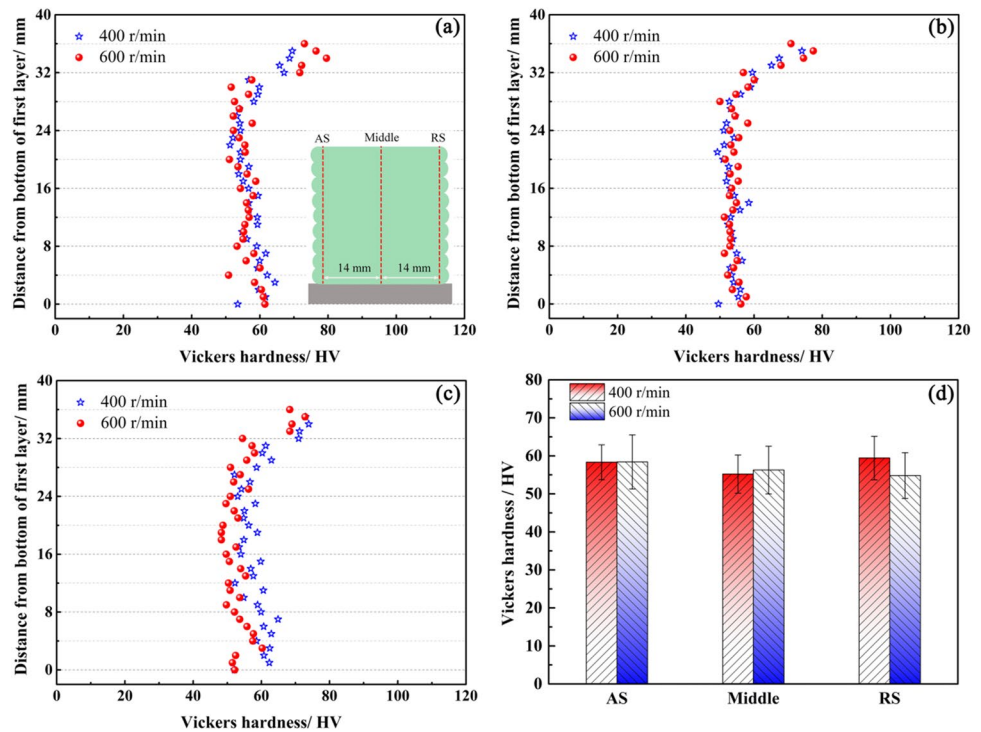


Fig. 8 Tensile test results along the build direction of final deposits at 400 r/min and 600 r/min; a engineering stress–engineering strain curves, b appearance of the samples after tensile tests, c tensile strength, d elongation at break, e 0.2% proof stress, and f calculated average values

produced at different rotation speeds. The appearance of sample no. 6 and no. 11 after tensile testing is presented in Fig. 8(b). Although the tensile strength of sample no. 11 at 400 r/min is equivalent to that at 600 r/min, the elongation

at break is 7% greater. This specimen has obvious necking deformation prior to tensile failure (Fig. 8(b)).

Figure 8(c), (d), and (e) shows the average values of tensile strength, elongation at break, and 0.2% proof stress,

respectively. The tensile strength of sample no. 2 through no. 13 at 400 r/min can reach more than 150 MPa, and the 0.2% proof stress is more than 100 MPa. However, the elongation at break of nos. 2, 3, and 4 is all less than 7%, while the other samples range from 10.6% to 19.5%. Sample no. 5 to 13 should have a solid bonding, which means that the width for excellent bonding at 400 r/min should be about 20 mm. The tensile strength of sample no. 2 to No. 14 can all be over 100 MPa at 600 r/min, while the 0.2% proof stress of sample no. 3 to no. 12 can all be above 100 MPa. The elongation at break of sample no. 5 to no. 13 is more than 7%. Sample nos. 5 to 12 should achieve good bonding, and the interface width for good bonding at 600 r/min is about 17.5 mm.

Figure 8(f) shows the calculated average values of tensile properties of the specimens achieving good bonding. The tensile strength, 0.2% proof stress, and elongation at break can reach 47.4%, 32.0%, and 103% of the base metal, respectively. However, these values of final deposits produced at 600 r/min can achieve 45.2%, 32.1%, and 66.3% of the starting material.

4 Discussion

4.1 Interfacial bonding mechanism with a featureless tool

In this study, the nine-layer final deposits with a layer width (W_d) of around 32 mm and a layer thickness (T_d) of about 4 mm were successfully produced by the FEAM process. The consumable feed rod is completely converted into the deposited layer using the processing parameters of this work, with no additional material transformed to flash. The volumetric deposition rate (DR_{vol}) [40] during FEAM can be expressed by the product of the deposited cross-section area (S_d) and the tool traverse speed (v), that is, the deposition volume per unit time as depicted by Eq. (1).

$$DR_{vol} [\text{cm}^3/\text{min}] = S_d v \quad (1)$$

The schematic representation of plasticized metal flow within different zones at 400 and 600 r/min is depicted in

Fig. 9 Schematic representation of the material flow in different zones of the cross-section of the deposited layers at 400 r/min (a) and 600 r/min (b)

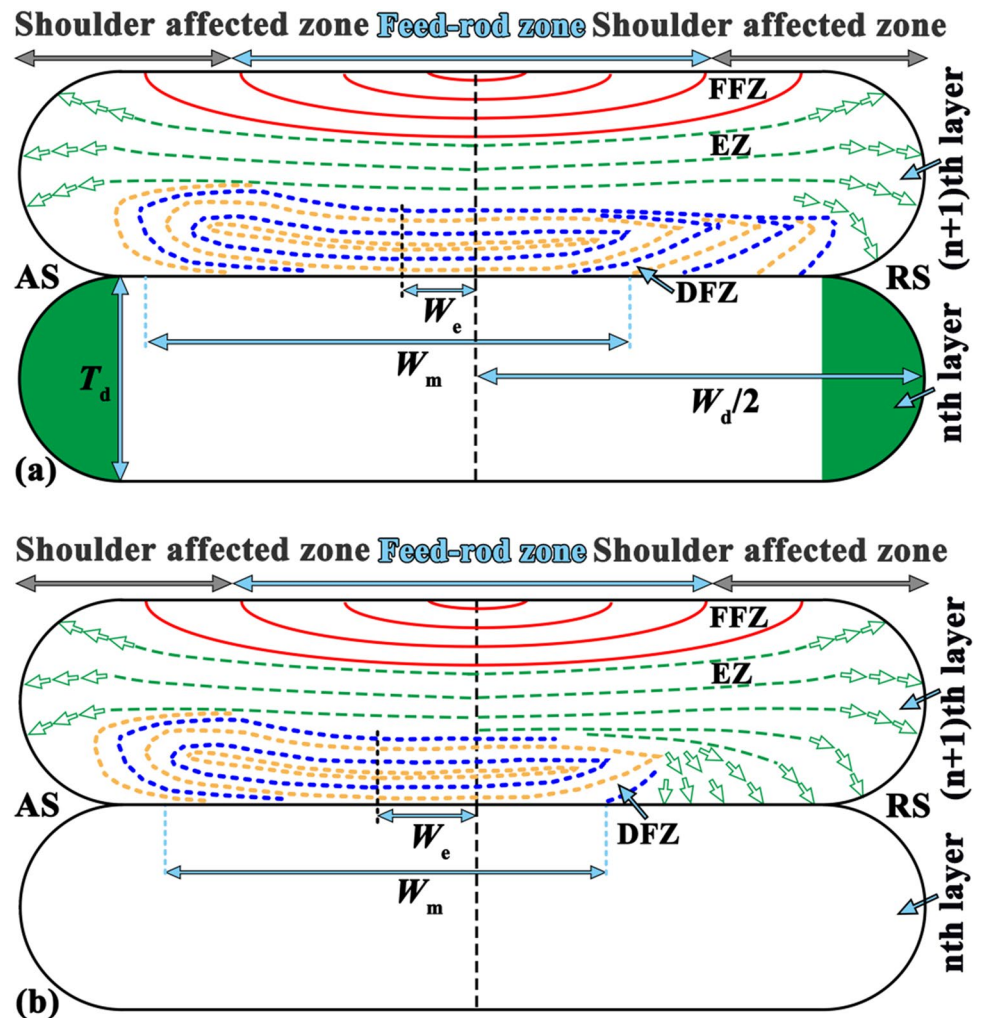


Fig. 9. The ends of the deposition layer (see green semicircles in Fig. 9(a)) can be approximated as two semicircles with diameters equal to the layer thickness. The deposited cross-section area can be calculated by adding the area of these two semicircles to the rectangle area between the two semicircles, as given in Eq. (2).

$$S_d = \pi(T_d/2)^2 + (W_d - T_d)T_d \quad (2)$$

According to Eqs. (1) and (2), the deposition rate in this study is up to 6.2 kg/h ($\rho_{6061-Al} = 2.75 \text{ g/cm}^3$ [41]), much higher than that of the AFSD method currently publicly reported [21]. Compared to wire arc additive manufacturing (WAAM), which is also considered to be an effective process for the preparation of large-size components [42], the deposition rate in this work is 2.8 times that of the previously reported WAAM of Al–Mg–Mn alloy [43]. Although the final deposits were obtained at such high deposition rates, just a part of the deposited material is effectively joined. As such, the material utilization ratio (η_m) is given by the ratio between the effectively bonded width (W_m) and the W_d , as expressed by Eq. (3).

$$\eta_m = W_m/W_d \quad (3)$$

From Eq. (3), it can be obtained that the η_m at 600 r/min is only 54.7%, while it increases to 62.5% when the tool rotation speed is reduced to 400 r/min. In a previous study [44], the η_m of final deposits produced by friction stir additive manufacturing using rod form of Al 6061 alloy was reported to be 42.7%. The improvement in material utilization is directly related to the interfacial bonding mechanism at different tool rotation speeds.

This high deposition rate in this study is mainly due to the fact that the thickness of the individual layers is up to 4 mm. Because of the inhomogeneous thermo-mechanical coupling effects encountered at different locations during deposition, the flow traces of the plasticized material within the layer display considerable difference, as depicted in Fig. 9. For this reason, each layer of final deposits was divided into three zones and designated DFZ, FFZ, and EZ, respectively. The DFZ was closest to the frictional interface, where the highest temperature and the greatest amount of plastic deformation took place. This part of the metal was deposited by the shear deformation of the rotating shoulder, mainly from the softened metal in direct contact with the substrate or the previously deposited layer. The cross-section of the deposited layer is symmetrical about the centerline of the consumed feed rod. However, the flow features formed in DFZ (see yellow- and blue-dotted lines in Fig. 9) exhibit significant asymmetry, and the center of the formed complete ellipses is always on AS. Here, the vertical distance between the

center of the complete ellipses and the centerline of the deposited layer is denoted as W_e .

The metal of the FFZ was initially subjected to extrusion deformation of the unaffected consumable feed rod, followed by the frictional and shear action of the rotating shoulder. As a result, this region formed the flow features depicted by the red lines in Fig. 9. The centerline of these flow characteristics corresponded approximately to the centerline of the deposited layer, which differed from the DFZ. In the EZ, the plasticized materials were indirectly subjected to extrusion deformation of the unaffected feed rod and rotating shoulder so that they flew from the semi-enclosed space consisting of DFZ and FFZ to the two ends of the deposited layer (see green-dotted lines in Fig. 9). Since the flow features in the DFZ did not cover the entire joining area, some of the metal in the EZ was deposited at the interface near the RS. This region, where the interface formed by the plasticized materials extruded from the EZ is located, was prone to the formation of voids and kissing bond defects because these metals flown from the EZ were subjected to lower shear stress and upsetting force. The width of this area, which was susceptible to the formation of defects, increased significantly when the rotational speed of the tool increased to 600 r/min because the material did not flow sufficiently during deposition. Accordingly, the width of the DFZ became much smaller, and the value of W_e became much larger (see Fig. 9(b)). For the above reasons, the effective joining width of the interface at 600 r/min is only 17.5 mm, and the joining quality is much worse. The final deposits obtained at 400 rpm improved the bonding quality compared to those produced at 600 rpm, as the plasticized metal at the interface was strongly forced to produce the entire flow rings of plastic materials in DFZ.

Differences in bonding mechanisms at different rotation speeds resulted in differences in the preferential orientation of the grains. FEAM developed a plastic deformation process in addition to the thermal process compared to fusion-based additive manufacturing. The textures of each area were determined mainly by the plastic deformation process. The proportions of recrystallization, deformation, and shear textures in the different regions (Table 3) were counted, as depicted in Fig. 10. Compared to DFZ, the percentage of deformation textures in FFZ reduced from 14.1 to 8.2%, and the proportion of recrystallized textures decreased from 17.9 to 0%. The number of shear textures grew from 8.9 to 27.4%. Since the EZ was not subjected to significant shear effects, it exhibited deformation and recrystallization textures predominantly. It is also noted that the microstructural features of the EZ differ significantly at different rotation speeds. The dynamic recrystallization fraction of the freshly deposited metal, i.e., the ninth layer, was much higher at 400 r/min with an 8.9% higher recrystallization fraction than at 600

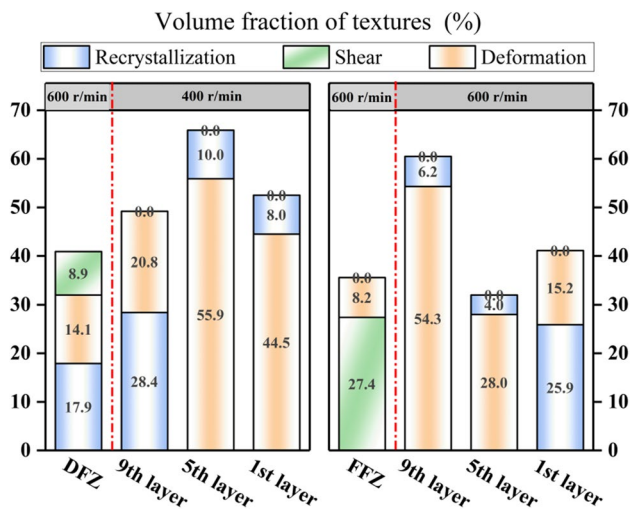


Fig. 10 The proportion of recrystallization, deformation, and shear textures in different regions of final deposits

r/min. When the rotation speed increased to 600 r/min, the dynamic recovery process became even more prominent, with an 8.7% higher substructured fraction than at 400 r/min.

Differences in bonding mechanisms at different rotation speeds also lead to differences in grain refinement and restoration mechanisms. The materials of the first and fifth layers were exposed to repeated thermal and plastic deformation processes. During the subsequent deposition process, the temperature, and the strain rate experienced in these regions were gradually reduced relative to the newly deposited material (the ninth layer). As a result, the thermomechanical coupling conditions encountered in these locations are insufficient to drive additional dynamic and static recrystallization processes during multilayer deposition. Dynamic recovery and static recovery following the dynamic recovery processes accompanied by subgrain coarsening and grain growth predominated at 400 r/min.

The proportion of the subgrain in these regions increased to 9.4% and 13.4%, respectively (Table 2). The total grain size increased significantly due to subgrain coarsening and grain growth at 600 r/min. However, the subgrain fraction did not increase, implying that the stored energy gained through plastic deformation was insufficient to drive the dynamic and static recovery processes during multilayer deposition [45, 46].

4.2 Improved interlayer bonding by regulating interfacial formation

The findings of this study are compared to the tensile properties of as-printed 6061 Al alloys manufactured using different additive manufacturing processes [4, 6, 15, 16, 26, 44], as depicted in Fig. 11. The tensile strength along

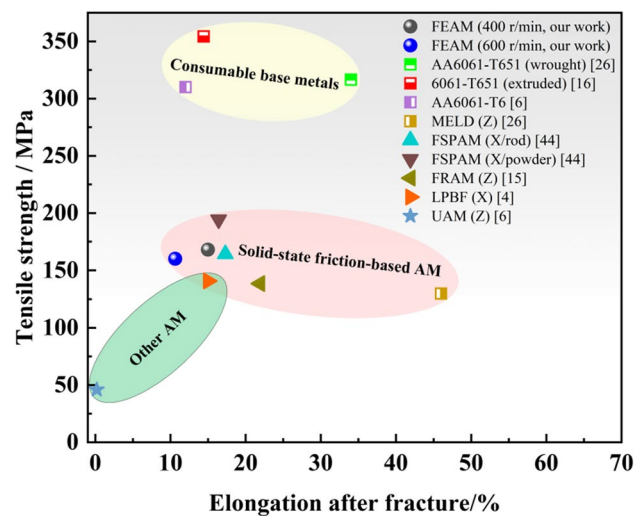


Fig. 11 Comparison of the tensile properties of as-printed commercial 6061-Al alloy produced by FEAM and other additive manufacturing processes

the Z-direction here has a significant advantage over that in the X-direction of the 6061 Al alloy fabricated by the laser powder bed fusion (LPBF) process, and the elongation after fracture is comparable [4]. The tensile strength of 6061-Al produced by ultrasonic additive manufacturing (UAM) was less than 50 MPa, and the elongation at break was less than 0.2% [6]. Compared to the multilayer deposits fabricated with MELD [26], the tensile strength and 0.2% proof stress in this study were greater than 38.1 MPa and 42.5 MPa, respectively, and the elongation after fracture is approximately half. It should be noted that the tensile properties in the X-direction of the 6061 Al prepared by FSPAM in powder form were slightly better than those obtained in this work, but the deposition efficiency only reached 59.8% [44]. The elongation after fracture along the Z-direction of the final builds produced by FEAM was unsatisfactory due to the use of a featureless tool during deposition. The featureless tool produced a relatively planar planar interface with low plastic deformation capability and no mixing of the materials along the Z-direction [16, 17].

In summary, the final deposits produced by FEAM at a high deposition rate of 6.2 kg/h from a commercial 6061 Al alloy have overall better mechanical properties than those of other additive manufacturing processes. The strong flow of the deposited metal at DFZ at 400 r/min results in improved interfacial development, although no mixing of the deposited metal with the previous layer occurs at any rotation speed. However, the material utilization achieved in this work is rather poor. The main processing parameters of FEAM that determine the forming quality and bonding strength are tool rotation speed, traverse speed, tool axial force, and pre-set thickness. During deposition, DFZ in the newly deposited

layer underwent significant dynamic recrystallization and replaced the original interface for successful bonding. If the tool rotation speed and traverse speed remain constant, increasing the axial force or decreasing the pre-set thickness of the deposited layer should promote the flow of the plastic materials in DFZ. The changes to the above processing parameters are expected to improve the quality and width of the interfacial bond and avoid the formation of kiss bond defects, thereby increasing material utilization and plastic deformability of the interface.

5 Conclusions

- 1) The force-controlled FEAM successfully produced the final deposits with nine layers of 6061 Al alloy at a deposition rate of 6.2 kg/h under the rotation speeds of 400 and 600 r/min. Each layer of final deposits produced at 400 r/min was constant in width and thickness, approximately 32 mm wide and 4 mm thick.
- 2) The flow characteristics of the plasticized materials during deposition varied considerably at different tool rotation speeds. The effective joining width at the interfaces was determined by the breadth of the entire flow rings generated in DFZ. Material utilization was significantly greater at the lower rotation speed of 400 r/min and could be as high as 62.5%.
- 3) Irrespective of the rotation speed, the dynamic recovery and subsequent static recovery, accompanied by sub-grain coarsening and grain growth, predominated in EZ after several thermal cycles and plastic deformation. Grain refinement in EZ was most pronounced at 400 rpm, with an average grain size of about $6.0 \pm 3.3 \mu\text{m}$. The preferred orientation of the grains was more evident at 400 r/min, and the volume fractions of the deformation and recrystallization textures were higher than 49.2%.
- 4) Tensile properties in the build direction at 400 r/min are superior to those at 600 r/min, with R_m , $R_{p0.2}$, and A reaching 168.0 MPa, 106.4 MPa, and 15%, respectively.

Funding This work was supported by the [National Natural Science Foundation of China] under [Grant numbers 52175356 and 51775371], [Tianjin Natural Science Foundation] under [Grant number 19JCZDJC39200], and [Tianjin Research Innovation Project for Postgraduate Students] under [Grant number 2021YJSO2B03].

Data availability The raw/processed data required to reproduce these findings cannot be shared at this time as the data also forms part of an ongoing study.

Declarations

Ethics approval Not applicable.

Consent to participate Not applicable.

Consent for publication All authors have read and agreed to the published version of the paper.

Conflict of interest The authors declare no competing interests.

References

1. Boyer RR (1996) An overview on the use of titanium in the aerospace industry. *Mater Sci Eng A* 213:103–114. [https://doi.org/10.1016/0921-5093\(96\)10233-1](https://doi.org/10.1016/0921-5093(96)10233-1)
2. Williams JC, Starke EA Jr (2003) Progress in structural materials for aerospace systems. *Acta Mater* 51:5775–5799. <https://doi.org/10.1016/j.actamat.2003.08.023>
3. Shimizu S, Fujii HT, Sato YS, Kokawa H, Sriraman MR, Babu SS (2014) Mechanism of weld formation during very-high-power ultrasonic additive manufacturing of Al alloy 6061. *Acta Mater* 74:234–243. <https://doi.org/10.1016/j.actamat.2014.04.043>
4. Uddin SZ, Murr LE, Terrazas CA, Morton P, Roberson DA, Wicker RB (2018) Processing and characterization of crack-free aluminum 6061 using high-temperature heating in laser powder bed fusion additive manufacturing. *Addit Manuf* 22:405–415. <https://doi.org/10.1016/j.addma.2018.05.047>
5. Martin JH, Yahata BD, Hundley JM, Mayer JA, Schaedler TA, Pollock TM (2017) 3D printing of high-strength aluminium alloys. *Nature* 549:365–369. <https://doi.org/10.1038/nature23894>
6. Sridharan N, Gussev M, Seibert R, Parish C, Norfolk M, Terrani K, Babu SS (2016) Rationalization of anisotropic mechanical properties of Al-6061 fabricated using ultrasonic additive manufacturing. *Acta Mater* 117:228–237. <https://doi.org/10.1016/j.actamat.2016.06.048>
7. Utyaganova VR, Filippov AV, Shamarin NN, Vorontsov AV, Savchenko NL, Fortuna SV, Gurianov DA, Chumaevskii AV, Rubtsov VE, Tarasov SY (2020) Controlling the porosity using exponential decay heat input regimes during electron beam wire-feed additive manufacturing of Al-Mg alloy. *Int J Adv Manuf Technol* 108:2823–2838. <https://doi.org/10.1007/s00170-020-05539-9>
8. Yu HZ, Jones ME, Brady GW, Griffiths RJ, Garcia D, Rauch HA, Cox CD, Hardwick N (2018) Non-beam-based metal additive manufacturing enabled by additive friction stir deposition. *Scr Mater* 153:122–130. <https://doi.org/10.1016/j.scriptamat.2018.03.025>
9. Gussev MN, Sridharan N, Thompson Z, Terrani KA, Babu SS (2018) Influence of hot isostatic pressing on the performance of aluminum alloy fabricated by ultrasonic additive manufacturing. *Scr Mater* 145:33–36. <https://doi.org/10.1016/j.scriptamat.2017.10.004>
10. Palanivel S, Nelaturu P, Glass B, Mishra RS (2015) Friction stir additive manufacturing for high structural performance through microstructural control in an Mg based WE43 alloy. *Mater Des* 65:934–952. <https://doi.org/10.1016/j.matdes.2014.09.082>
11. Zhao Z, Yang X, Li S, Li D (2019) Interfacial bonding features of friction stir additive manufactured build for 2195–T8 aluminum-lithium alloy. *J Manuf Process* 38:396–410. <https://doi.org/10.1016/j.jmapro.2019.01.042>
12. Roodgari MR, Jamaati R, Jamshidi Aval H (2020) Fabrication of a 2-layer laminated steel composite by friction stir additive

- manufacturing. *J Manuf Process* 51:110–121. <https://doi.org/10.1016/j.jmapro.2020.01.031>
13. Calvert JR (2015) Microstructure and mechanical properties of WE43 alloy produced via additive friction stir technology[D]. Virginia Tech
 14. Blindheim J, Grong Ø, Aakenes UR, Welo T, Steinert M (2018) Hybrid metal extrusion & bonding (HYB) - a new technology for solid-state additive manufacturing of aluminium components. *Procedia Manuf* 26:782–789. <https://doi.org/10.1016/j.promfg.2018.07.092>
 15. Xie R, Shi Y, Liu H, Chen S (2021) A novel friction and rolling based solid-state additive manufacturing method: microstructure and mechanical properties evaluation. *Mater Today Commun* 29:103005. <https://doi.org/10.1016/j.mtcomm.2021.103005>
 16. Tang W, Yang X, Tian C, Xu Y (2022) Microstructural heterogeneity and bonding strength of planar interface formed in additive manufacturing of Al–Mg–Si alloy based on friction and extrusion. *Int J Miner Metall Mater* 29:1755–1769. <https://doi.org/10.1007/s12613-022-2506-4>
 17. Tang W, Yang X, Tian C, Gu C (2022) Effect of rotation speed on microstructure and mechanical anisotropy of Al-5083 alloy builds fabricated by friction extrusion additive manufacturing. *Mater Sci Eng A* 860:144237. <https://doi.org/10.1016/j.msea.2022.144237>
 18. Chaudhary B, Jain NK, Murugesan J, Patel V (2022) Exploring temperature-controlled friction stir powder additive manufacturing process for multi-layer deposition of aluminum alloys. *J Mater Res Technol* 20:260–268. <https://doi.org/10.1016/j.jmrt.2022.07.049>
 19. Chen H, Chen J, Meng X, Xie Y, Huang Y, Xu S, Zhao Y (2022) Wire-based friction stir additive manufacturing toward field repairing. *Weld J* 101:249–252. <https://doi.org/10.29391/2022.101.019>
 20. Martin LP, Luccitti A, Walluk M (2022) Repair of aluminum 6061 plate by additive friction stir deposition. *Int J Adv Manuf Technol* 118:759–773. <https://doi.org/10.1007/s00170-021-07953-z>
 21. Rivera OG, Allison PG, Brewer LN, Rodriguez OL, Jordon JB, Liu T, Whittington WR, Martens RL, McClelland Z, Mason CJT, Garcia L, Su JQ, Hardwick N (2018) Influence of texture and grain refinement on the mechanical behavior of AA2219 fabricated by high shear solid state material deposition. *Mater Sci Eng A* 724:547–558. <https://doi.org/10.1016/j.msea.2018.03.088>
 22. Priedeman JL, Phillips BJ, Lopez JJ, Tucker Roper BE, Hornbuckle BC, Darling KA, Jordon JB, Allison PG, Thompson GB (2020) Microstructure development in additive friction stir-deposited Cu. *Metals (Basel)* 10:1538. <https://doi.org/10.3390/met10111538>
 23. Garcia D, Hartley WD, Rauch HA, Griffiths RJ, Wang R, Kong ZJ, Zhu Y, Yu HZ (2020) In situ investigation into temperature evolution and heat generation during additive friction stir deposition: a comparative study of Cu and Al–Mg–Si. *Addit Manuf* 34:101386. <https://doi.org/10.1016/j.addma.2020.101386>
 24. Rivera OG, Allison PG, Jordon JB, Rodriguez OL, Brewer LN, McClelland Z, Whittington WR, Francis D, Su J, Martens RL, Hardwick N (2017) Microstructures and mechanical behavior of Inconel 625 fabricated by solid-state additive manufacturing. *Mater Sci Eng A* 694:1–9. <https://doi.org/10.1016/j.msea.2017.03.105>
 25. Agrawal P, Haridas RS, Yadav S, Thapliyal S, Gaddam S, Verma R, Mishra RS (2021) Processing-structure-property correlation in additive friction stir deposited Ti-6Al-4V alloy from recycled metal chips. *Addit Manuf* 47:102259. <https://doi.org/10.1016/j.addma.2021.102259>
 26. Rutherford BA, Avery DZ, Phillips BJ, Rao HM, Doherty KJ, Allison PG, Brewer LN, Brian Jordon J (2020) Effect of thermo-mechanical processing on fatigue behavior in solid-state additive manufacturing of Al–Mg–Si alloy. *Metals (Basel)* 10:1–17. <https://doi.org/10.3390/met10070947>
 27. Phillips BJ, Avery DZ, Liu T, Rodriguez OL, Mason CJT, Jordon JB, Brewer LN, Allison PG (2019) Microstructure-deformation relationship of additive friction stir-deposition Al–Mg–Si. *Materials* 7:100387. <https://doi.org/10.1016/j.mtla.2019.100387>
 28. Perry MEJ, Griffiths RJ, Garcia D, Sietins JM, Zhu Y, Yu HZ (2020) Morphological and microstructural investigation of the non-planar interface formed in solid-state metal additive manufacturing by additive friction stir deposition. *Addit Manuf* 35:101293. <https://doi.org/10.1016/j.addma.2020.101293>
 29. Julien SE, Nourian-Avval A, Liang W, Schwartz T, Ozdemir OC, Müftü S (2022) Bulk fracture anisotropy in cold-sprayed Al 6061 deposits. *Eng Fract Mech* 263:108301. <https://doi.org/10.1016/j.engfracmech.2022.108301>
 30. Sitdikov O, Sakai T, Avtokratova E, Kaibyshev R, Tsuzaki K, Watanabe Y (2008) Microstructure behavior of Al–Mg–Sc alloy processed by ECAP at elevated temperature. *Acta Mater.* <https://doi.org/10.1016/j.actamat.2007.10.029>
 31. EN ISO 6892–1:2019 - Metallic materials - tensile testing - part 1: method of test at room temperature (ISO 6892–1:2019). <https://www.iso.org/obp/ui/#iso:std:iso:6892:-1:ed-3:v1:en>. Accessed 21 2019
 32. Abdollahzadeh A, Bagheri B, Abbasi M, Kokabi AH, Moghaddam AO (2021) Comparison of the weldability of AA6061-T6 joint under different friction stir welding conditions. *J Mater Eng Perform* 30:1110–1127. <https://doi.org/10.1007/s11665-020-05379-4>
 33. Vidakis N, Petousis M, Mountakis N, Kechagias JD (2022) Optimization of friction stir welding for various tool pin geometries : the weldability of polyamide 6 plates made of material extrusion additive manufacturing. *Int J Adv Manuf Technol* 2931–2955 <https://doi.org/10.1007/s00170-022-10675-5>
 34. Bagheri B, Abbasi M, Dadaei M (2020) Mechanical behavior and microstructure of AA6061-T6 joints made by friction stir vibration welding. *J Mater Eng Perform* 29:1165–1175. <https://doi.org/10.1007/s11665-020-04639-7>
 35. Agrawal P, Haridas RS, Agrawal P, Mishra RS (2022) Deformation based additive manufacturing of a metastable high entropy alloy via additive friction stir deposition. *Addit Manuf* 60:103282. <https://doi.org/10.1016/j.addma.2022.103282>
 36. Agrawal P, Haridas RS, Yadav S, Thapliyal S, Dhal A, Mishra RS (2023) Additive friction stir deposition of SS316: effect of process parameter on microstructure evolution. *Mater Charact* 195:112470. <https://doi.org/10.1016/j.matchar.2022.112470>
 37. Engler O, Hirsch J (2002) Texture control by thermomechanical processing of AA6xxx Al–Mg–Si sheet alloys for automotive applications - a review. *Mater Sci Eng A* 336:249–262. [https://doi.org/10.1016/S0921-5093\(01\)01968-2](https://doi.org/10.1016/S0921-5093(01)01968-2)
 38. Wu PD, MacEwen SR, Lloyd DJ, Neale KW (2004) Effect of cube texture on sheet metal formability. *Mater Sci Eng A* 364:182–187. <https://doi.org/10.1016/j.msea.2003.08.020>
 39. Tangen S, Sjølstad K, Furu T, Nes E (2010) Effect of concurrent precipitation on recrystallization and evolution of the P-texture component in a commercial Al–Mn alloy. *Metall Mater Trans A Phys Metall Mater Sci* 41:2970–2983. <https://doi.org/10.1007/s11661-010-0265-8>
 40. Gandra J, Krohn H, Miranda RM, Vilac P, Quintino L, Santos JF (2014) Friction surfacing — a review. *J Mater Process Technol* 214:1062–1093. <https://doi.org/10.1016/j.jmatprotec.2013.12.008>
 41. Liu W, Huang S, Du S, Gao T, Zhang Z, Chen X, Huang L (2022) The Effects of heat treatment on microstructure and mechanical properties of selective laser melting 6061 aluminum alloy. *Micromachines* 13:1059. <https://doi.org/10.3390/mi13071059>
 42. Murr LE, Gaytan SM, Ramirez DA, Martinez E, Hernandez J, Amato KN, Shindo PW, Medina FR, Wicker RB (2012) Metal fabrication by additive manufacturing using laser and electron beam melting technologies. *J Mater Sci Technol* 28:1–14. [https://doi.org/10.1016/S1005-0302\(12\)60016-4](https://doi.org/10.1016/S1005-0302(12)60016-4)
 43. Panchenko O, Kurushkin D, Mushnikov I, Khismatullin A, Popovich A (2020) A high-performance WAAM process for Al–Mg–Mn using controlled short-circuiting metal transfer at increased

- wire feed rate and increased travel speed. *Mater Des* 195:109040. <https://doi.org/10.1016/j.matdes.2020.109040>
44. Chaudhary B, Jain NK, Murugesan J, Sathiaraj D (2023) Study of microstructure evolution and mechanical properties in friction stir based additive multi-layer manufacturing of Al 6061 alloy: effect of feedstock material form and heat treatment. *Mater Today Commun* 34:105156. <https://doi.org/10.1016/j.mtcomm.2022.105156>
45. Griffiths RJ, Garcia D, Song J, Vasudevan VK, Steiner MA, Cai W, Yu HZ (2021) Solid-state additive manufacturing of aluminum and copper using additive friction stir deposition: process-microstructure linkages. *Materialia* 15:100967. <https://doi.org/10.1016/j.mtla.2020.100967>
46. Rollett A, Humphreys F, Rohrer GS, Hatherly M (2004) *Recrystallization and related annealing phenomena*, 2nd edn. Elsevier

Publisher's note Springer Nature remains neutral with regard to jurisdictional claims in published maps and institutional affiliations.

Springer Nature or its licensor (e.g. a society or other partner) holds exclusive rights to this article under a publishing agreement with the author(s) or other rightsholder(s); author self-archiving of the accepted manuscript version of this article is solely governed by the terms of such publishing agreement and applicable law.